

THERMODYNAMICS OF COMPLEX SOLIDS

Thermal desulfurization of pyrite: An in situ high-T neutron diffraction and DTA–TGA study

Hongwu Xu^{1,a)}, Xiaofeng Guo^{1,b)} , Lani A. Seaman², Aaron J. Harrison², Stephen J. Obrey², Katharine Page³

¹Earth and Environmental Sciences Division, Los Alamos National Laboratory, Los Alamos, New Mexico 87545, USA

²Chemistry Division, Los Alamos National Laboratory, Los Alamos, New Mexico 87545, USA

³Neutron Scattering Division, Oak Ridge National Laboratory, Oak Ridge, Tennessee 37831, USA

^{a)}Address all correspondence to this author. e-mail: hxu@lanl.gov

^{b)}Present address: Department of Chemistry, Washington State University, Pullman, Washington 99164, USA.

Received: 31 March 2019; accepted: 30 April 2019

To study thermal desulfurization of pyrite (FeS_2), we conducted in situ neutron diffraction experiments in the temperature range 298–1073 K. On heating, pyrite remained stable up to 773 K, at which it started to decompose into pyrrhotite (Fe_{1-x}S) and S_2 gas. Rietveld analysis of the neutron data from 298 to 773 K allowed determination of the thermal expansion coefficient of pyrite (space group $Pa\bar{3}$) to be $\alpha_v = 3.7456 \times 10^{-5} \text{ K}^{-1}$, which largely results from the expansion of the Fe–S bond. With further increase in temperature to 1073 K, all the pyrite transformed to pyrrhotite (Fe_{1-x}S) at 873 K. Unit-cell parameters of Fe_{1-x}S (space group $P6_3/mmc$) increase on heating and decrease on cooling. However, the rates in cell expansion are larger than those in contraction. This hysteresis behavior can be attributed to continuous desulfurization of pyrrhotite (i.e., x in Fe_{1-x}S decreases) with increasing temperature until the stoichiometric troilite (FeS) was formed at 1073 K. On cooling, troilite underwent a magnetic transition to an orthorhombic structure (space group $Pnma$) between 473 and 573 K. In addition, using differential thermal analysis (DTA) and thermogravimetric analysis (TGA) implemented with a differential scanning calorimeter, we performed kinetic measurements of pyrite decomposition. Detailed peak profile and Arrhenius ($k = A \exp(-E_a/RT)$) analyses yielded an activation energy E_a of $302.3 \pm 28.6 \text{ kJ/mol}$ (based on DTA data) or $302.5 \pm 26.4 \text{ kJ/mol}$ (based on TGA data) and a $\ln(A)$ of 35.3 ± 0.1 .

Introduction

As the most common sulfide in the Earth's crust [1], pyrite (FeS_2) occurs in a wide variety of geological settings, including sedimentary deposits, hydrothermal veins, and metamorphic rocks. Industrially, pyrite is the raw ore mineral for manufacturing sulfuric acid [2] and recovering Au [3], and is a semiconducting, optical material itself [4]. On the other hand, because pyrite exists in coal and oil/gas shale as an accessory phase, the associated fossil fuel extraction may lead to emission of SO_2 or SO_3 when pyrite is oxidized, thereby posing environmental concerns [5].

Because of its importance to many geological and industrial processes, thermal decomposition of pyrite has been studied using a number of experimental techniques, especially thermogravimetric analysis (TGA) and X-ray diffraction (XRD)

[5, 6, 7, 8, 9]. The results demonstrate that the phases formed from pyrite decomposition and its reaction kinetics are highly dependent on experimental conditions, particularly the gas atmosphere used (O_2 , N_2 , air, inert gas, vacuum, etc.). In oxidative environments, pyrite is easily oxidized to iron oxides, such as hematite ($\alpha\text{-Fe}_2\text{O}_3$) and magnetite (Fe_3O_4). Under nonoxidizing conditions, pyrrhotite (Fe_{1-x}S with varying x) becomes the major product. Most of the earlier studies used isothermal or non-isothermal TGA at different temperatures or heating rates, respectively, followed by ex situ characterization of the post-TGA samples by XRD and other techniques. These measurements yielded kinetic parameters of pyrite thermal decomposition, such as the activation energy, which are sensitive to gas species and their partial pressures.

The primary aim of this study was to examine structural transformation and evolution when pyrite undergoes decomposition or, more precisely, desulfurization upon heating under vacuum using in situ high-temperature neutron diffraction [10, 11, 12, 13, 14]. In particular, the composition and structure of the nonstoichiometric pyrrhotite (Fe_{1-x}S) vary systematically with increasing temperature and/or time. In addition, previous studies show that the thermal decomposition of pyrite progresses with a clear boundary between the unreacted pyrite and the formed product layer of pyrrhotite, as revealed by scanning electron microscopy (SEM) [15]. Because neutrons are highly penetrating (versus X-rays), the use of neutron diffraction allows for investigation of the structures of both pyrrhotite and its parent pyrite when the transformation is incomplete. Moreover, as neutrons, through their magnetic moment, can directly probe magnetic structures of materials, neutron diffraction is an ideal tool for studying magnetic transitions, e.g., those occurring in troilite (FeS) [16, 17, 18, 19, 20, 21, 22, 23, 24, 25]. Another goal of this work was to characterize the kinetics of pyrite desulfurization using DTA–TGA (differential thermal analysis–thermogravimetric analysis), which can be correlated with the structural information revealed by neutron diffraction.

In this study, in situ high-temperature neutron diffraction was conducted on pyrite using a pulsed neutron source at temperatures up to 1073 K under vacuum. On heating, pyrite remained stable up to 773 K, at which it started to decompose into pyrrhotite and S_2 gas. On further heating, all the pyrite transformed to pyrrhotite at 873 K, and the nonstoichiometric pyrrhotite continued to undergo desulfurization, i.e., decrease in x in Fe_{1-x}S , with increasing temperature until the stoichiometric troilite (FeS) was formed at 1073 K. On cooling, troilite underwent a magnetic transition to an orthorhombic phase between 473 and 573 K, accompanied by a volume reduction. Rietveld analyses of the neutron data allow determination of structural parameters of these phases as a function of temperature. The structural mechanisms underlying pyrite desulfurization and related processes are discussed. In addition, to determine the kinetics of pyrite desulfurization, we performed DTA–TGA measurements in the same temperature range of 298–1073 K with different heating rates of 5, 10, 20, and 40 K/min under an argon atmosphere. Arrhenius analyses of the data yielded an activation energy E_a of 302.3 ± 28.6 kJ/mol (based on DTA data) or 302.5 ± 26.4 kJ/mol (based on TGA data) and a $\ln(A)$ of 35.3 ± 0.1 .

Results and discussion

Rietveld analysis of neutron diffraction data

We analyzed the obtained high-temperature neutron diffraction data using the Rietveld method [26]. Structural parameters of pyrite (FeS_2) and its decomposed pyrrhotite (Fe_{1-x}S) and

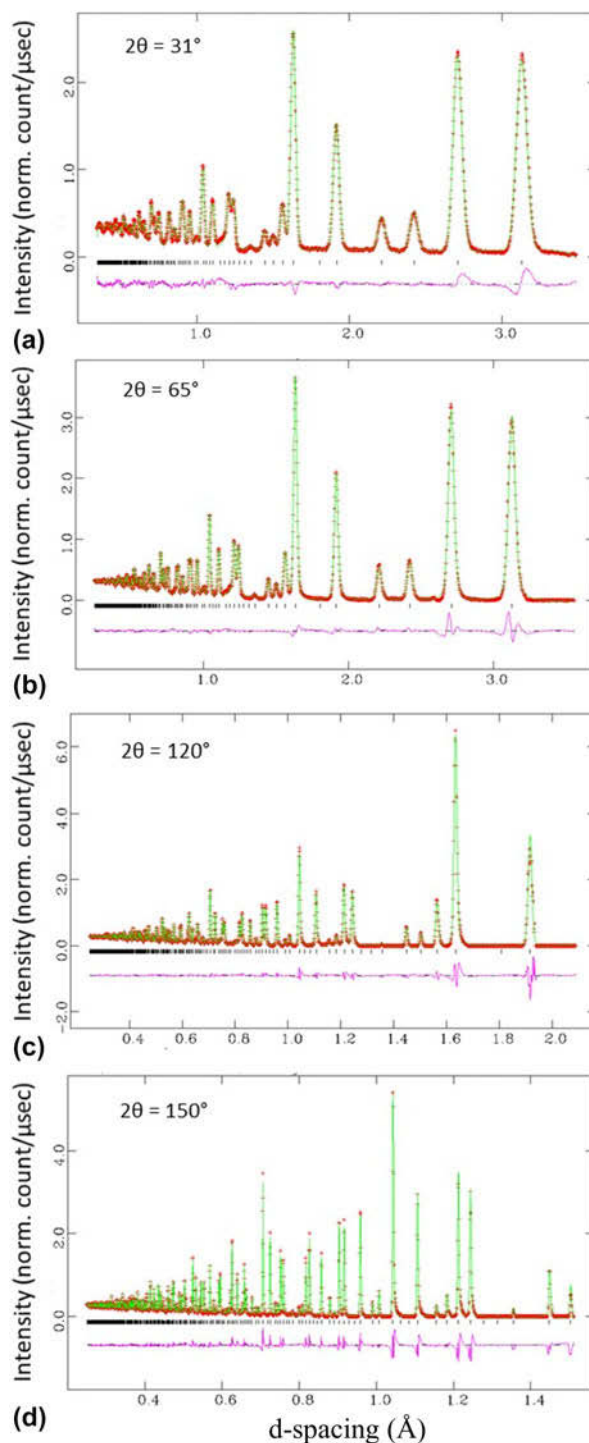


Figure 1: Fitted neutron diffraction patterns of FeS_2 collected at (a) $2\theta = 31^\circ$, (b) $2\theta = 65^\circ$, (c) $2\theta = 120^\circ$, and (d) $2\theta = 150^\circ$ at 298 K. Data are shown as red plus signs, and the solid green curve is the best fit to the data. Tick marks below the pattern show the positions of allowed reflections, and the lower curve represents the difference between the observed and calculated profiles.

troilite (FeS) at different temperatures were derived. Figure 1 shows a representative set of fitted patterns (298 K), and Table I lists unit-cell parameters and refinement agreement

TABLE I: Unit-cell parameters and refinement agreement indices of FeS₂ and/or Fe_{1-x}S.

<i>T</i> (K)	<i>a</i> (Å)	<i>V</i> (Å ³)	<i>a</i> (Å)	<i>b</i> (Å)	<i>c</i> (Å)	<i>V</i> (Å ³)	<i>R</i> _{wp} (%)
298 ^a	5.42215(6)	159.410(5)	8.1
373 ^a	5.42696(6)	159.834(5)	8.1
473 ^a	5.43353(7)	160.415(6)	7.8
573 ^a	5.44012(7)	161.000(6)	7.8
673 ^a	5.44716(7)	161.625(6)	7.6
773 ^b	5.45430(12)	162.262(11)	3.5198(1)	...	5.7176(3)	61.347(4)	5.7
873 ^c	3.5485(2)	...	5.7845(3)	63.080(9)	5.2
973 ^c	3.5671(2)	...	5.8301(4)	64.246(10)	5.1
1073 ^c	3.5808(3)	...	5.8651(5)	65.127(12)	5.4
973 ^d	3.5737(2)	...	5.8485(4)	64.685(10)	5.3
873 ^d	3.5655(2)	...	5.8309(3)	64.195(8)	5.3
773 ^d	3.5573(1)	...	5.8150(2)	63.728(6)	5.5
673 ^d	3.5484(1)	...	5.8006(2)	63.251(5)	5.7
573 ^d	3.5372(1)	...	5.7906(2)	62.744(5)	6.1
473 ^e	5.8074(3)	3.5070(2)	6.0833(4)	123.89(2)	8.5
373 ^e	5.8197(3)	3.4844(3)	6.0219(5)	122.11(2)	8.1

^aHeating: pyrite (FeS₂, space group *Pa* $\bar{3}$).

^bHeating: a mixture of pyrite and pyrrhotite with the refined molar ratio FeS₂:Fe_{1-x}S = 0.173:0.827.

^cHeating: pyrrhotite (Fe_{1-x}S, space group *P6*₃/*mmc*).

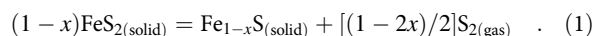
^dCooling: troilite (FeS, space group *P6*₃/*mmc*).

^eCooling: troilite (FeS, space group *Pnma*).

indices of FeS₂ and/or Fe_{1-x}S on heating to 1073 K and then cooling to 373 K.

Thermal decomposition of pyrite under vacuum

Our high-temperature neutron diffraction patterns indicate that FeS₂ was stable from 298 to 673 K (Fig. 2(a)). However, the sample partially decomposed into pyrrhotite (Fe_{1-x}S) and S₂ (g) when the temperature reached 773 K [Fig. 2(b)], as shown by Eq. (1):



The refined molar ratio FeS₂:Fe_{1-x}S at 773 K is 0.173:0.827. On further heating to 873 K, all the pyrite transformed to pyrrhotite [Fig. 2(c)]. Thus, the onset temperature of the decomposition (*T*_d) lies between 673 and 773 K. As shown in previous studies, the decomposition temperature may vary depending on the heating paths (heating rate and dwell time) used and the partial S₂ pressure. Our lower *T*_d compared with previously reported values (e.g., *T*_d = 799.35 K [6]) may be due to the longer dwell time needed for neutron data collection and/or the lower partial pressure (the sample can was not fully sealed, and the sample was under vacuum). As shown later, this *T*_d is also much lower than those (around 900 K) measured with DTA-TGA at different heating rates under Ar atmosphere, as there was no dwelling during the later measurements. In addition, as revealed by SEM [10], pyrite decomposition involves formation of a core-shell structure consisting of pyrrhotite shell and unreacted pyrite core. Thus,

the grain size of pyrite may play a role in the kinetics of its decomposition.

Thermal expansion of pyrite

The obtained unit-cell parameter *a* and cell volume *V* of pyrite from 298 to 773 K are plotted in Figs. 3(a) and 3(b), respectively. On heating, cell parameter *a* increases, and thus cell volume *V* also increases, as revealed by previous XRD measurements [27]. To obtain the coefficients of thermal expansion (CTEs), we fitted these data to linear relations:

$$a = [6.73(6) \times 10^{-5}]T + 5.4019(3) \quad (R^2 = 0.9997) \quad ,$$

$$V = [5.97(6) \times 10^{-3}]T + 157.61(3) \quad (R^2 = 0.9996) \quad .$$

The mean CTEs of FeS₂ in the temperature range 298–773 K are $\alpha_a = 6.73 \times 10^{-5} \text{ K}^{-1}$ and $\alpha_V = 5.97 \times 10^{-3} \text{ K}^{-1}$.

The unit-cell dimensional variations with temperature can be interpreted in terms of the pyrite structure. Pyrite has a cubic structure with the space group *Pa* $\bar{3}$ [Fig. 4(a)]. In the structure, each pair of S atoms forms a dumbbell, and each low-spin divalent Fe is coordinated to six S atoms, forming a corner-sharing [FeS₆] octahedral framework [1]. As shown in Fig. 3(c), with increasing temperature, whereas the S–S bond length remains approximately unchanged (or even slightly decreases), the Fe–S bond length increases steadily, which is due to the different bonding characters of S–S and Fe–S. Thus, the thermal expansion of pyrite is largely due to the Fe–S bond lengthening or [FeS₆] octahedral expansion.

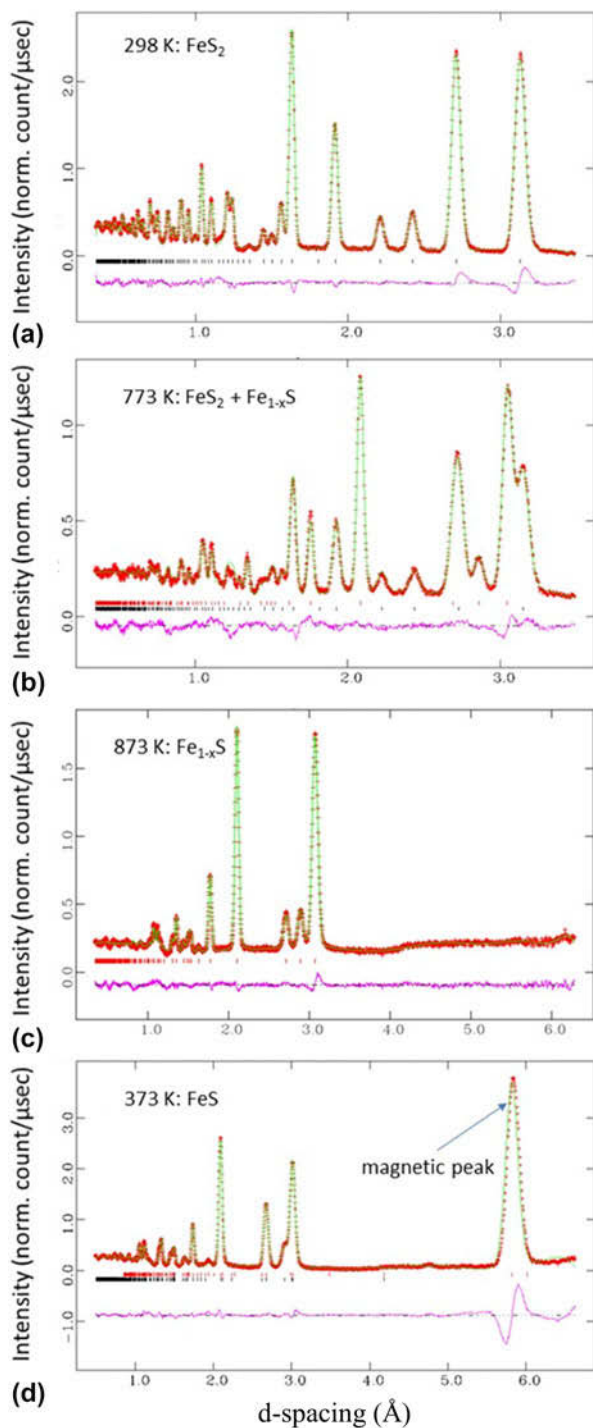


Figure 2: Selected neutron diffraction patterns ($2\theta = 31^\circ$) on heating pyrite to 1073 K and then cooled down to 373 K: (a) 298 K: pyrite, FeS_2 ; (b) heating to 773 K: partial decomposition of pyrite into pyrrhotite, $\text{FeS}_2 + \text{Fe}_{1-x}\text{S}$; (c) heating to 873 K: complete decomposition of pyrite into pyrrhotite, Fe_{1-x}S ; and (d) cooling to 373 K: troilite, FeS ($Pnma$ with a magnetic structure).

Figure 3(d) shows variation of isotropic displacement factors (U_{iso}) of Fe and S with temperature. At a given temperature, $U_{\text{iso}}(\text{Fe}) < U_{\text{iso}}(\text{S})$. With increasing temperature, the U_{iso} values for both Fe and S become larger. This is

consistent with the general trend that the lighter the atom and the higher the temperature, the larger the magnitude of atomic vibration.

Evolution of pyrrhotite

Even after the pyrite completely converted to pyrrhotite (Fe_{1-x}S) at 873 K, the desulfurization process continued. Figures 5a, 5b and 5c plot variation of cell parameters a , c , and cell volume V , respectively, of pyrrhotite (the NiAs-type structure, space group $P6_3/mmc$) as a function of temperature. With increasing temperature from 773 to 1073 K, a , c , and V all increase. Upon cooling from 1073 K, they decrease. However, the rates of lattice contraction on cooling are much smaller than those of lattice expansion on heating. This behavior can be interpreted by continuous desulfurization of pyrrhotite (i.e., x in Fe_{1-x}S decreases, although the x values were not determined due to the limited resolution of neutron diffraction data) on heating until the stoichiometric troilite (FeS) was formed at 1073 K. Because of the removal of S from the Fe_{1-x}S structure (equivalent to addition of Fe or decrease in x), desulfurization of pyrrhotite leads to expansion of its unit cell. Furthermore, increasing temperature results in conventional thermal expansion of pyrrhotite. The summation of these two effects causes larger rates of lattice expansion on heating. By contrast, during the subsequent cooling, because the composition of FeS remains constant (no desulfurization), the rates of lattice contraction are much lower. In other words, if there were no desulfurization on heating, the rates of expansion in a , c , and V would be the same as those of contraction in a , c , and V , respectively.

To obtain the CTEs of hexagonal troilite FeS , we fitted its cell data collected on cooling from 1073 to 573 K (below which a phase transition occurs, see below) to linear relations:

$$a = [8.6(3) \times 10^{-5}]T + 3.490(3) \quad (R^2 = 0.9947) \quad ,$$

$$c = [1.52(6) \times 10^{-4}]T + 5.700(5) \quad (R^2 = 0.9928) \quad ,$$

$$V = [4.767(4) \times 10^{-3}]T + 60.03(4) \quad (R^2 = 0.9997) \quad .$$

The mean CTEs of FeS in the temperature range 573–1073 K are $\alpha_a = 8.60 \times 10^{-5} \text{ K}^{-1}$, $\alpha_c = 15.2 \times 10^{-5} \text{ K}^{-1}$, and $\alpha_V = 4.77 \times 10^{-3} \text{ K}^{-1}$. Because the CTE along the c -axis is almost two times that along the a -axis, the thermal expansion of FeS is anisotropic (consistent with previous XRD measurements [28]), which may be explained in terms of the layer-like nature of its structure [Fig. 4(b)]. On the other hand, similar to pyrite, the thermal expansion of FeS is largely due to the Fe–S bond lengthening or $[\text{FeS}_6]$ octahedral expansion [Fig. 5(d)] (although the rate of increase in Fe–S in FeS_2 with increasing temperature is smaller, presumably due to the occurrence of S_2 dumbbells in the pyrite structure).

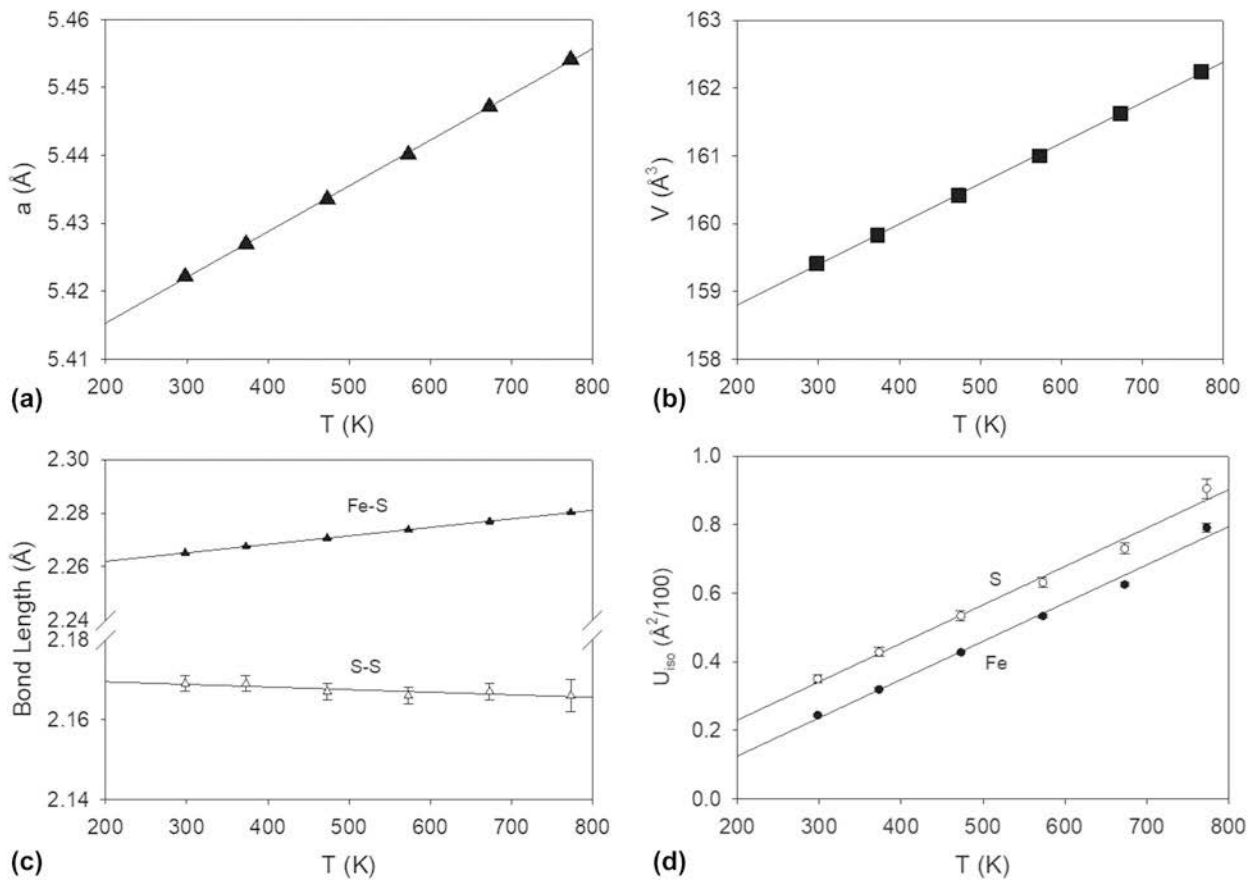


Figure 3: Variations of (a) cell parameters a , (b) cell volume V , (c) Fe-S and S-S bond lengths, and (d) isotropic thermal parameters (U_{180}) for Fe and S of pyrite as a function of temperature. The lines are the best fits to the data. For the data point without an error bar, its uncertainty is smaller than the size of the symbol.

Magnetic transition in troilite

Upon cooling troilite (FeS) from 573 to 473 K, a strong neutron diffraction peak around 5.8 Å appeared, and this peak persisted on further cooling to 373 K [Fig. 2(d)]. This phenomenon can be attributed to a magnetic transition to the orthorhombic phase (space group $Pnma$) with a magnetic moment of Fe along the b -axis [18]. Note that this structure is MnP type and has been observed at high pressure [18, 24, 25]. This transformation is also manifested by an increase in the slope of variations in cell volume with decreasing temperature [Fig. 5(e)]. More specifically, in addition to the magnetic ordering, the structure becomes denser and decreases its symmetry from hexagonal ($P6_3/mmc$) to orthorhombic ($Pnma$).

Kinetics of pyrite desulfurization

To characterize the kinetics of pyrite desulfurization, we conducted a series of DTA-TGA experiments from room temperature up to 1073 K with heating rates, ϕ , of 5, 10, 20, and 40 K/min under an argon atmosphere [Figs. 6(a)–6(c)]. Note that compared with the neutron diffraction experiments described above, the heating rates for the DTA-TGA kinetic

measurements were higher, there was no dwelling at a given temperature, and argon atmosphere (instead of vacuum) was used. Thus, the results from these two sets of experiments cannot be compared in a point-by-point fashion. The thermal decomposition, described by Eq. (1), produces one dominant endothermic peak and the corresponding weight loss. The slower weight loss after reaction (1) is complete [Fig. 6(c)] is due to the continuous desulfurization of pyrrhotite, as revealed by neutron diffraction. With increasing the heating rate, the heat flow-time peak becomes sharper [Fig. 6(a)], the decomposition peak temperature systematically increases [Fig. 6(b)], and so does the weight loss temperature [Fig. 6(c)]. The heating rate-dependent weight loss leads to variation in the x value of the final decomposed pyrrhotite $Fe_{1-x}S$ at 1073 K based on Eq. (1). As shown in Fig. 6(d), x exhibits an approximately linear relation with the heating rate. Because there were no dwellings during the DTA-TGA measurements (i.e., the total duration for each measurement was much shorter), the final decomposed $Fe_{1-x}S$ did not reach the stoichiometric FeS, as in the neutron experiments. In addition, the DTA (heat flow - temperature) peak becomes larger with an increase in the heating rate [Fig. 6(b)]. To

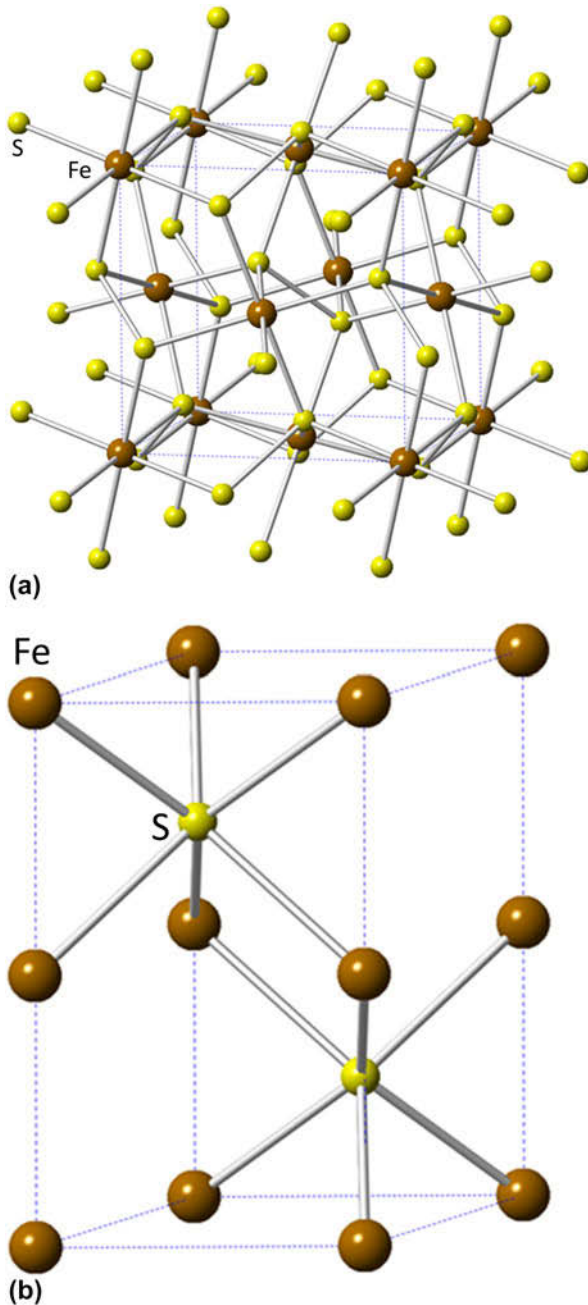


Figure 4: Crystal structures of (a) pyrite (FeS₂, space group $Pa\bar{3}$) and (b) pyrrhotite (Fe_{1-x}S, high-temperature polymorph with the NiAs-type structure, space group $P6_3/mmc$). Brown balls represent Fe atoms, and yellow balls represent S atoms. Dashed lines define the unit cell.

characterize the heat flow profile of each heating segment, we denote T_m as the temperature of the sample at the peak of the heat flow, which also increases as the heating rate increases. The order of reaction (n), which characterizes how the reaction rate relates to the concentration of the reactant (pyrite here), can be determined from the asymmetry of the heat flow peak [29, 30], which is described by a shape index S defined as the ratio of absolute values of slopes of the tangents

to the DTA peak curves at the inflection points. The reaction order can then be derived as $n = \sqrt{S/0.63}$ [30], and the calculated n values are listed in Table II with an average value of 0.59 ± 0.05 . The activation energy E_a can be derived from the equation referenced by Kissinger [30]:

$$\frac{d(\ln \phi/T_m^2)}{d(1/T_m)} = -\frac{E_a}{R} \quad (2)$$

The activation energy of pyrite desulfurization is thus obtained from the slope value of the linear fitting Eq. (2) using DTA data [Fig. 7(a)] to be 302.3 ± 28.6 kJ/mol, or TGA data [Fig. 7(b)] to be 302.5 ± 26.4 kJ/mol. Having known the values of E_a , n , T_m , and ϕ , the frequency factor A , i.e., the pre-exponential factor after integration of Eq. (2), which represents the frequency of collisions between reactants, can be determined via Eq. (3), and its natural logarithm can be calculated for each DTA-TGA experiment shown in Table II with an average value of $\ln(A) = 35.3 \pm 0.1$,

$$\frac{E_a \phi}{RT_m^2} = A \left[1 + (1-n) \frac{2RT_m}{E_a} \right] \cdot e^{-E_a/RT_m} \quad (3)$$

The Arrhenius plot for the pyrite decomposition reaction can also be made [Fig. 7(c)] based on Eq. (4), where $\ln(k)$ has a linear relationship against $1/T$:

$$k = Ae^{-E_a/RT} \quad (4)$$

The obtained kinetic parameters are in good agreement with those from previous studies [8, 15, 31, 32] (Table II).

Conclusions

Using time-of-flight neutron diffraction coupled with Rietveld analysis, we have investigated thermal desulfurization of FeS₂ under vacuum in the temperature range 298–1073 K. On heating, pyrite remained stable up to 773 K, at which it started to decompose into Fe_{1-x}S and S₂ gas. Rietveld analysis of the neutron data from 298 to 773 K allowed determination of the thermal expansion coefficient of pyrite, which largely results from the expansion of Fe-S bond. With further increase in temperature to 1073 K, all the pyrite transformed to Fe_{1-x}S at 873 K. Unit-cell parameters of Fe_{1-x}S increase on heating and decrease on cooling. However, the rates in cell expansion are larger than those in contraction. This hysteresis behavior can be attributed to continuous desulfurization of Fe_{1-x}S with increasing temperature until the stoichiometric troilite FeS was formed at 1073 K. On cooling, troilite underwent a magnetic transition to an orthorhombic structure with a magnetic moment of Fe along the b -axis between 473 and 573 K. In

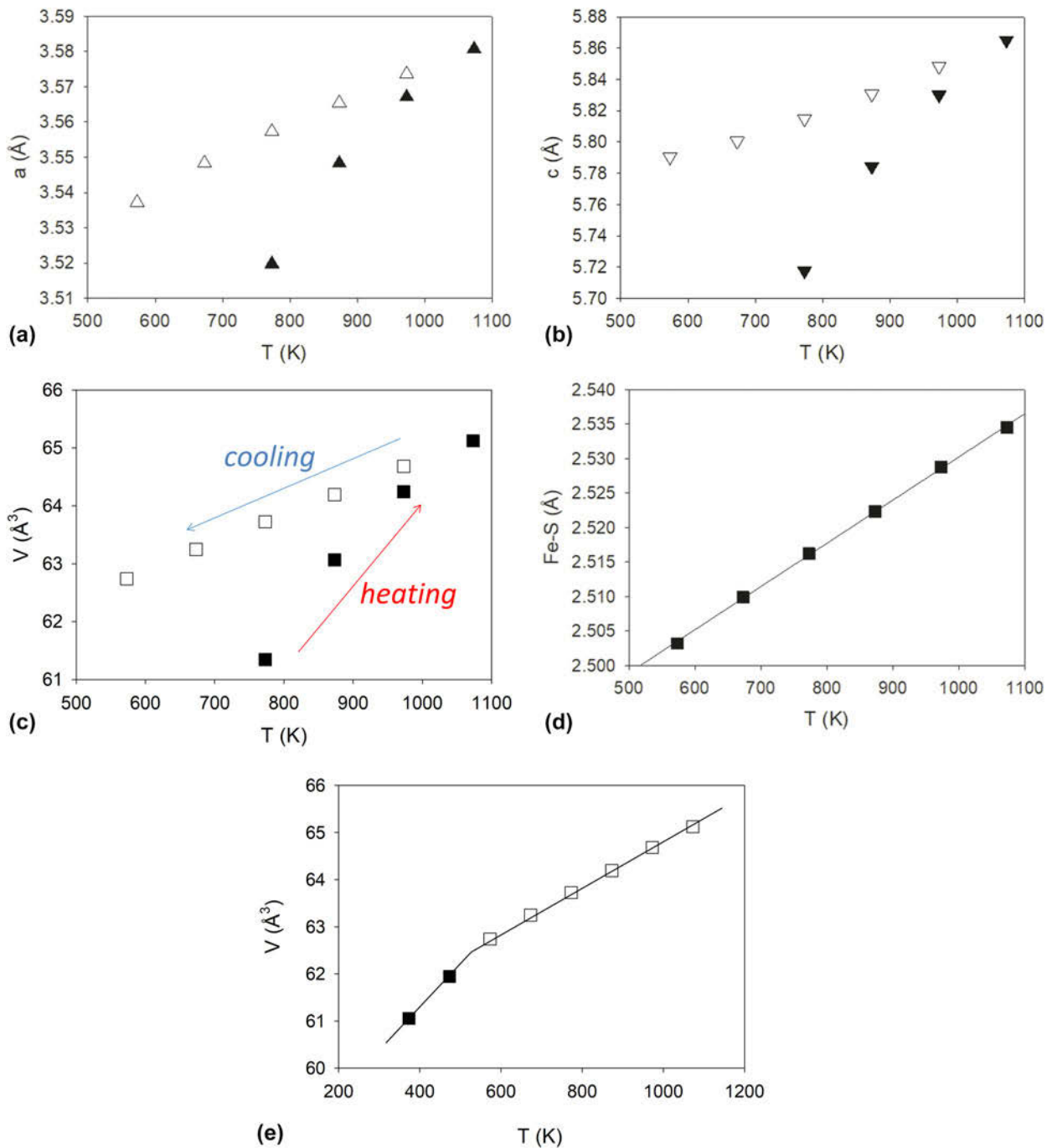


Figure 5: Variation of cell parameters (a) a , (b) c , (c) cell volume V , and (d) Fe-S bond length of pyrrhotite as a function of temperature. (e) Variation of cell volume V of troilite as a function of temperature. The uncertainty of each data point is smaller than the size of the symbol. The slope change is due to the hexagonal-orthorhombic transition.

addition, using DTA-TGA, we characterized the kinetics of pyrite decomposition under an argon atmosphere. Arrhenius analyses yielded an activation energy E_a of 302.3 ± 28.6 kJ/mol (based on DTA data) or 302.5 ± 26.4 kJ/mol (based on TGA data) and a $\ln(A)$ of 35.3 ± 0.1 . This study represents an example of combining in situ structural characterization with kinetic/thermodynamic measurements

to determine the structure-stability relationships of materials [33, 34, 35, 36, 37].

Methods and approaches

Neutron diffraction

Time-of-flight neutron diffraction experiments were performed at the Nanoscale-Ordered Materials Diffractometer

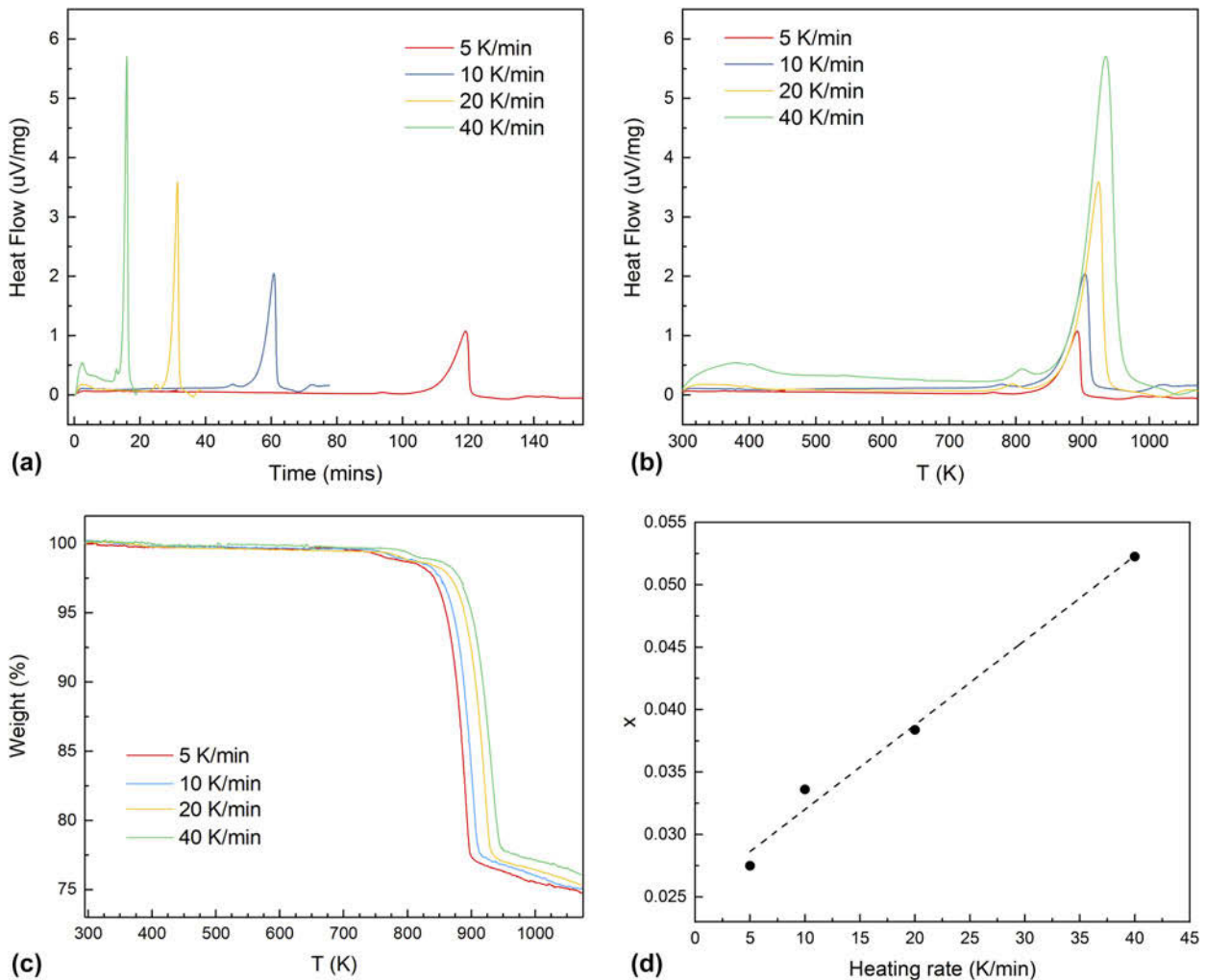


Figure 6: DTA (a and b) and TGA (c) curves of FeS₂ from room temperature to 1073 K with heating rates of 5, 10, 20, and 40 K/min under an argon atmosphere. (d) Variation of *x* in Fe_{1-x}S as a function of the heating rate.

TABLE II: Kinetic parameters of pyrite desulfurization derived from DTA–TGA data up to 1073 K under Ar atmosphere.

Heating rate (K/min)	<i>T_m</i> (K)	<i>n</i>	ln(<i>A</i>)	<i>E_a</i> (kJ/mol)
5	892.0	0.535	35.2	...
10	903.6	0.616	35.4	...
20	924.1	0.615	35.1	...
40	934.8	0.797 ^a	35.4	...
				302.3 ± 28.6 ^b
Average	...	0.59 ± 0.05	35.3 ± 0.1	302.5 ± 26.4 ^c 280–297 ^d

^aNot used in the *n* value averaging.

^bFrom the DTA data.

^cFrom the TGA data.

^dFrom Refs. 8, 15, 31, and 32.

(NOMAD) beamline of the Spallation Neutron Source, Oak Ridge National Laboratory [38]. NOMAD is a high-flux, medium-resolution diffractometer that uses a large bandwidth of neutron energies and extensive detector coverage,

affording a broad range of scattering angles (*Q*-range) and peak resolutions ($\delta Q/Q$) for structural determinations of crystalline, nanocrystalline, and amorphous materials. A pyrite powder sample (Sigma-Aldrich, St. Louis, MO, ~325 mesh, 99.8% trace metals basis) was put into a silica-glass ampoule, which was in turn placed in a vanadium can of 0.95 cm diameter. (The use of the silica-glass ampoule was to avoid corrosive reaction of the vanadium can with the evolved S₂ gas at high temperatures.) The can was then mounted in an ILL-type high-temperature furnace with vanadium heating elements and heatshields for contamination-free diffraction data collection. Data were collected under vacuum (<10⁻⁶ torr) on heating from 298 to 1073 K and then cooled down to 373 K with an interval of 100 K. For each temperature point, six detector banks with nominal diffraction angles of 7°, 15°, 31°, 65°, 120°, and 150° were simultaneously used. The heating rate during the 100-K intervals was ~5 K/min, and the dwell time at each targeted temperature was ~1 h for data

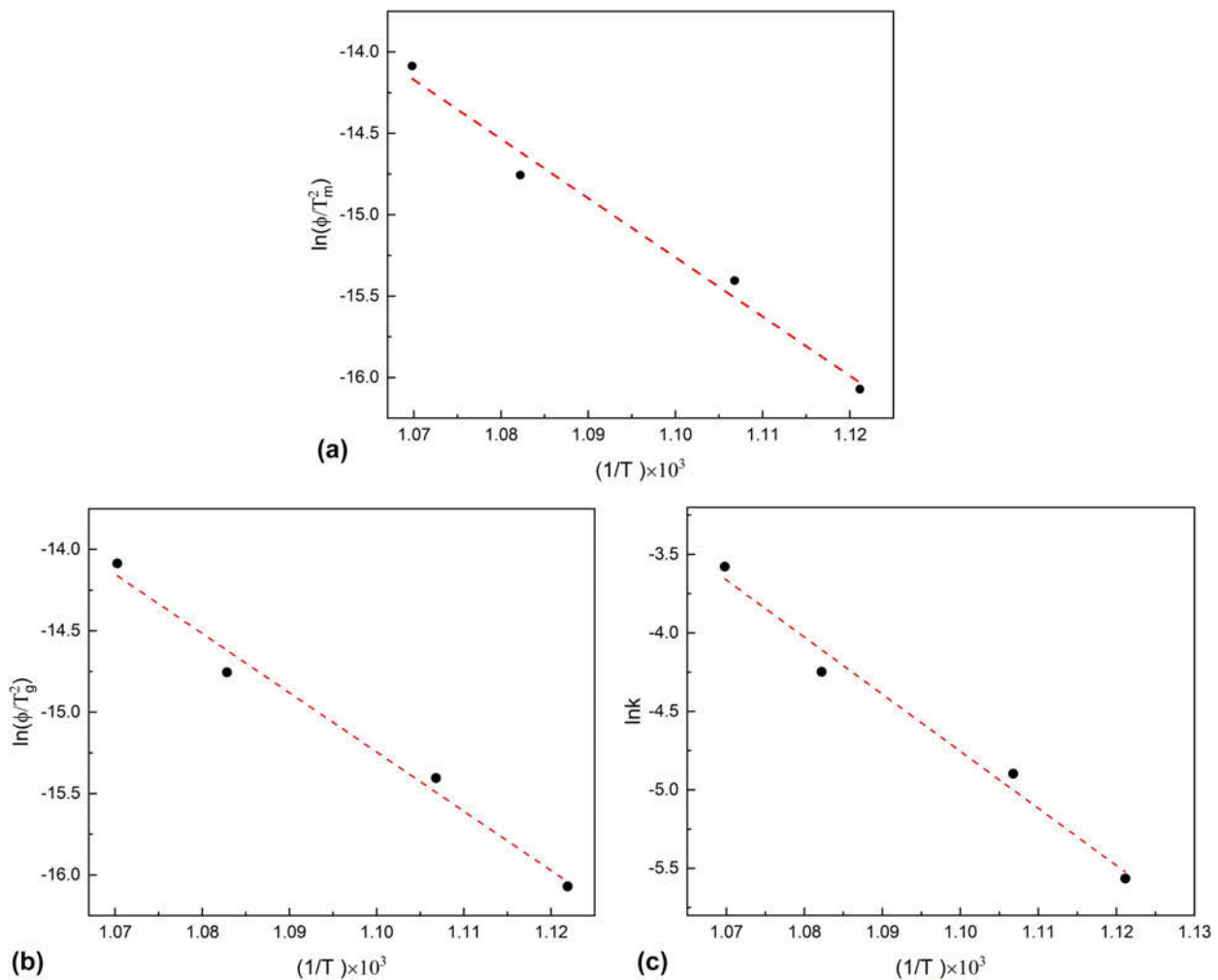


Figure 7: Linear fittings to derive the activation energy E_a of pyrite desulfurization from (a) DTA and (b) TGA data based on Eq. (2). (c) Arrhenius plot of pyrite desulfurization based on Eq. (4).

collection. One-hour background measurements were made for an empty vanadium can and empty instrument and were subtracted from the raw data.

Rietveld analysis

The obtained neutron data were analyzed using the Rietveld method with the General Structure Analysis System (GSAS) program of Larson and Von Dreele [39]. The starting structural parameters for FeS_2 at 298 K were taken from the study of Bayliss [40]. The starting parameters for Fe_{1-x}S (including hexagonal FeS, the NiAs-type structure, space group $P6_3/mmc$) at 773 K were taken from the study of Alsén [41]. The starting parameters for orthorhombic FeS at 473 K were taken from the study of Marshall et al. [18]. We used the refined structural parameters at a given temperature as the starting parameters for the next temperature point and continued this procedure systematically with increasing or decreasing temperature. For the run at 773 K, because a portion of the pyrite sample

decomposed into pyrrhotite (Fe_{1-x}S) and S_2 gas, we included pyrrhotite as a secondary phase in our Rietveld analysis. For each temperature point, four datasets from the detectors at $2\theta = 31^\circ, 65^\circ, 120^\circ,$ and 150° were simultaneously analyzed (the 7° and 15° datasets were not used because of their relatively low resolutions). The refinements proceeded as follows: after the scale factor and four background terms (Shifted Chebyshev function) for each histogram had converged, lattice parameters and phase fraction (for the run at 773 K) were added and optimized. Fourteen or eighteen additional background terms were then added for each histogram, and the peak profiles were fitted to a TOF profile function [42]. On convergence of the preceding parameters, atomic coordinates and atomic displacement parameters for Fe and S were refined.

Thermal analysis

High-temperature DTA–TGA measurements were conducted using a Netzsch simultaneous thermal analyzer (STA) 449

system. About 5–15 mg of the sample powders were packed in a graphite crucible. The loaded crucible, along with an empty graphite crucible, was then placed into the calorimeter and heated to 1073 K at a preset heating rate (5–40 K/min) under a flowing Ar atmosphere (90 mL/min). For baseline correction, an earlier scan using the empty graphite crucible was run under the same conditions. Temperature was calibrated against the melting points of several metal standards (e.g., In and Al). Sensitivity calibration was done using sapphire as the standard. Data collection and processing were performed using the Netzsch software (Netzsch Group, Selb, Germany) associated with the instrument. Detailed procedures have been described previously [43, 44, 45].

Acknowledgments

We thank the three anonymous reviewers for their helpful comments. This work was supported by the US Department of Energy (DOE) Energy Efficiency & Renewable Energy (EERE) program. This research used resources at the Spallation Neutron Source, a DOE Office of Science User Facility operated by the Oak Ridge National Laboratory. Los Alamos National Laboratory, an affirmative action/equal opportunity employer, is managed by Triad National Security, LLC, for the National Nuclear Security Administration of the U.S. Department of Energy under contract 89233218CNA000001.

References

- D.J. Vaughan:** Sulfide mineralogy and geochemistry. (*Rev. Mineral. Geochem.* Volume **61**, Mineralogical Society of America, Chantilly, VA, 2006) 714 pp.
- Z. Lin and U. Quarfort:** Predicting the mobility of Zn, Fe, Cu, Pb, Cd from roasted sulfide (pyrite) residues—A case study of wastes from the sulfuric acid industry in Sweden. *Waste Manage.* **16**, 671 (1996).
- J. Hiskey and M. Pritzker:** Electrochemical behavior of pyrite in sulfuric acid solutions containing silver ions. *J. Appl. Electrochem.* **18**, 484 (1988).
- A.S. Barnard and S.P. Russo:** Shape and thermodynamic stability of pyrite FeS₂ nanocrystals and nanorods. *J. Phys. Chem. C* **111**, 11742 (2007).
- G. Hu, K. Dam-Johansen, S. Wedel, and J.P. Hansen:** Decomposition and oxidation of pyrite. *Prog. Energy Combust. Sci.* **32**, 295 (2006).
- J. Deng, S. Wen, X. Chen, Y. Xian, and D. Wu:** Dynamic simulation of the thermal decomposition of pyrite under vacuum. *Metall. Mater. Trans. A* **45**, 2445 (2014).
- H.J. Hurst, J.H. Levy, and S.S.J. Warné:** The application of variable atmosphere thermomagnetometry to the thermal decomposition of pyrite. *React. Solids* **8**, 159 (1990).
- J.M. Lambert, G. Simkovich, and P.L. Walker:** The kinetics and mechanism of the pyrite-to-pyrrhotite transformation. *Metall. Mater. Trans. B* **29**, 385 (1998).
- S.K. Bhargava, A. Garg, and N.D. Subasinghe:** In situ high-temperature phase transformation studies on pyrite. *Fuel* **88**, 988 (2009).
- H. Xu, Y. Zhao, S.C. Vogel, L.L. Daemen, and D.D. Hickmott:** Anisotropic thermal expansion and hydrogen bonding behavior of portlandite: A high-temperature neutron diffraction study. *J. Solid State Chem.* **180**, 1519 (2007).
- H. Xu, Y. Zhao, J. Zhang, D.D. Hickmott, and L.L. Daemen:** In situ neutron diffraction study of deuterated portlandite Ca(OD)₂ at high pressure and temperature. *Phys. Chem. Miner.* **34**, 223 (2007).
- H.W. Xu, Y.S. Zhao, S.C. Vogel, D.D. Hickmott, L.L. Daemen, and M.A. Hartl:** Thermal expansion and decomposition of jarosite: A high-temperature neutron diffraction study. *Phys. Chem. Miner.* **37**, 73 (2010).
- H.W. Xu, G.C.C. Costa, C.R. Stanek, and A. Navrotsky:** Structural behavior of Ba_{1.24}Al_{2.48}Ti_{5.52}O₁₆ hollandite at high temperature: An in situ neutron diffraction study. *J. Am. Ceram. Soc.* **98**, 255 (2015).
- H.W. Xu, Y.S. Zhao, D.D. Hickmott, N.J. Lane, S.C. Vogel, J.Z. Zhang, and L.L. Daemen:** High-temperature neutron diffraction study of deuterated brucite. *Phys. Chem. Miner.* **40**, 799 (2013).
- Y. Hong and B. Fegley, Jr.:** The kinetics and mechanism of pyrite thermal decomposition. *Ber. Bunsenges. Phys. Chem.* **101**, 1870 (1997).
- A.F. Andresen:** Magnetic phase transitions in stoichiometric FeS studied by means of neutron diffraction. *Acta Chem. Scand.* **14**, 919 (1960).
- H. Wang and I. Salveson:** A review on the mineral chemistry of the non-stoichiometric iron sulphide, Fe_{1-x}S (0 ≤ x ≤ 0.125): Polymorphs, phase relations and transitions, electronic and magnetic structures. *Phase Transitions* **78**, 547 (2005).
- W.G. Marshall, R.J. Nelmes, J.S. Loveday, S. Klotz, J.M. Besson, G. Hamel, and J.B. Parise:** High-pressure neutron-diffraction study of FeS. *Phys. Rev. B* **61**, 11201 (2000).
- N.V. Baranov, P.N.G. Ibrahim, N.V. Selezneva, V.A. Kazantsev, A.S. Volegov, and D.A. Shishkin:** Crystal structure, phase transitions and magnetic properties of pyrrhotite-type compounds Fe_{7-x}Ti_xS₈. *Phys. B* **449**, 229 (2014).
- F. Li and H.F. Franzen:** From pyrrhotite to troilite—An application of the Landau theory of phase-transitions. *J. Alloys Compd.* **215**, L3 (1994).
- A.V. Powell, P. Vaquero, K.S. Knight, L.C. Chapon, and R.D. Sanchez:** Structure and magnetism in synthetic pyrrhotite Fe₇S₈: A powder neutron-diffraction study. *Phys. Rev. B* **70**, 014415, 1 (2004).
- C. Tenailleau, B. Etschmann, H. Wang, A. Pring, B.A. Grguric, and A. Studer:** Thermal expansion of troilite and pyrrhotite

- determined by in situ cooling (873 to 373 K) neutron powder diffraction measurements. *Mineral. Mag.* **69**, 205 (2005).
23. **J.P.R. de Villiers and D.C. Liles:** The crystal-structure and vacancy distribution in 6C pyrrhotite. *Am. Mineral.* **95**, 148 (2010).
 24. **H.E. King, Jr. and C.T. Prewitt:** High-pressure and high-temperature polymorphism of iron sulfide (FeS). *Acta Crystallogr., Sect. B: Struct. Crystallogr. Cryst. Chem.* **38**, 1877 (1982).
 25. **A.F. Andresen and P. Torbo:** Phase transitions in Fe_xS ($x = 0.90$ – 1.00) studied by neutron diffraction. *Acta Chem. Scand.* **21**, 2841 (1967).
 26. **H. Rietveld:** A profile refinement method for nuclear and magnetic structures. *J. Appl. Crystallogr.* **2**, 65 (1969).
 27. **S.B. Chrysta:** Thermal expansion of iron pyrites. *Trans. Faraday Soc.* **61**, 1811 (1965).
 28. **E.N. Selivanov, A.D. Vershinin, and R.I. Gulyaeva:** Thermal expansion of troilite and pyrrhotine in helium and air. *Inorg. Mater.* **39**, 1097 (2003).
 29. **W.W. Wendlandt:** Reaction kinetics by differential thermal analysis: A physical chemistry experiment. *J. Chem. Educ.* **38**, 571 (1961).
 30. **H.E. Kissinger:** Reaction kinetics in differential thermal analysis. *Anal. Chem.* **29**, 1702 (1957).
 31. **A.W. Coats and N.F.H. Bright:** The kinetics of the thermal decomposition of pyrite. *Can. J. Chem.* **44**, 1191 (1966).
 32. **L. Charpentier and P.J. Masset:** Thermal decomposition of pyrite FeS₂ under reducing conditions. *Mater. Sci. Forum* **654–656**, 2398 (2010).
 33. **R. Li, J. Zhang, R. Tan, F. Gerdes, Z. Luo, H. Xu, J.A. Hollingsworth, C. Klinke, O. Chen, and Z. Wang:** Competing interactions between various entropic forces toward assembly of Pt₃Ni octahedra into a body-centered cubic superlattice. *Nano Lett.* **16**, 2792 (2016).
 34. **B.L. Phillips, H. Xu, P.J. Heaney, and A. Navrotsky:** ²⁹Si and ²⁷Al MAS-NMR spectroscopy of β-eucryptite (LiAlSiO₄): The enthalpy of Si,Al ordering. *Am. Mineral.* **85**, 181 (2000).
 35. **J. Zhu, S. Du, X. Yu, J. Zhang, H. Xu, S.C. Vogel, T.C. Germann, J.S. Francisco, F. Izumi, K. Momma, Y. Kawamura, C. Jin, and Y. Zhao:** Encapsulation kinetics and dynamics of carbon monoxide in clathrate hydrate. *Nat. Commun.* **5**, 4128 (2014).
 36. **J. Zhang, A. Celestian, J.B. Parise, H. Xu, and P.J. Heaney:** A new polymorph of eucryptite (LiAlSiO₄), ε-eucryptite, and thermal expansion of α- and ε-eucryptite at high pressure. *Am. Mineral.* **87**, 566 (2002).
 37. **H. Xu, A. Navrotsky, M.D. Nyman, and T.M. Nenoff:** Thermochemistry of microporous silicotitanate phases in the Na₂O–Cs₂O–SiO₂–TiO₂–H₂O system. *J. Mater. Res.* **15**, 815 (2000).
 38. **J. Neufeind, M. Feygenson, J. Carruth, R. Hoffmann, and K.K. Chiple:** The Nanoscale ordered MATERIALS diffractometer NOMAD at the spallation neutron source SNS. *Nucl. Instrum. Methods Phys. Res., Sect. B* **287**, 68 (2012).
 39. **A.C. Larson and R.B. Von Dreele:** General structure analysis system (GSAS); Los Alamos National Laboratory Report LAUR. 86–748, Los Alamos, NM, 2004, 224 pp.
 40. **P. Bayliss:** Crystal structure refinement of a weakly anisotropic pyrite. *Am. Mineral.* **62**, 1168 (1977).
 41. **N. Alsén:** Röntgenographische Untersuchung der Kristallstrukturen von Magnetkies, Breithauptit, Pentlandit, Millerit und verwandten Verbindungen. *Geol. Fören. Förh.* **47**, 19 (1925).
 42. **R.B. Von Dreele, J.D. Jorgensen, and C.G. Windsor:** Rietveld refinement with spallation neutron powder diffraction data. *J. Appl. Crystallogr.* **15**, 581 (1982).
 43. **X. Guo, S.V. Ushakov, S. Labs, H. Curtius, D. Bosbach, and A. Navrotsky:** Energetics of metastudtite and implications for nuclear waste alteration. *Proc. Natl. Acad. Sci. U. S. A.* **111**, 17737 (2014).
 44. **X. Guo, D. Wu, H. Xu, P.C. Burns, and A. Navrotsky:** Thermodynamic studies of studtite thermal decomposition pathways via amorphous intermediates UO₃, U₂O₇, and UO₄. *J. Nucl. Mater.* **478**, 158 (2016).
 45. **X. Guo and H. Xu:** Enthalpies of formation of polyhalite: A mineral relevant to salt repository. *J. Chem. Thermodyn.* **114**, 44 (2017).